PCCP

PAPER

View Article Online
View Journal | View Issue

Cite this: *Phys. Chem. Chem. Phys.*, 2015, **17**, 4458

^{7}Li *in situ* 1D NMR imaging of a lithium ion battery†

S. Klamor,[ab] K. Zick,[c] T. Oerther,[c] F. M. Schappacher,[b] M. Winter[ab] and G. Brunklaus*[a]

Received 31st October 2014,
Accepted 5th January 2015

DOI: 10.1039/c4cp05021e

www.rsc.org/pccp

The spatial distribution of charge carriers in lithium ion batteries during current flow is of fundamental interest for a detailed understanding of transport properties and the development of strategies for future improvements of the electrolyte–electrode interface behaviour. In this work we explored the potential of ^{7}Li 1D *in situ* NMR imaging for the identification of concentration gradients under constant current load in a battery cell. An electrochemical cell based on PTFE body and a stack of glass microfiber discs that are soaked with a technically relevant electrolyte suitable for high-temperature application and squeezed between a Li metal and a nano-Si–graphite composite electrode was assembled to acquire ^{7}Li 1D *in situ* NMR profiles with an improved NMR pulse sequence as function of time and state of charge, thereby visualizing the course of ion concentration during charge and discharge. Surface localized changes of Li concentration were attributed to processes such as solid electrolyte interphase formation or full lithiation of the composite electrode. The method allows the extraction of lithium ion transport properties.

Introduction

The increasing demand for mobile energy storage solutions suitable for safe and durable operation of electric vehicles has fostered many research activities in the field of rechargeable batteries.[1–3] Currently, rechargeable lithium ion batteries constitute an industrial state-of-the-art technology that above all has enabled modern portable electronic devices such as digital cameras, mobile phones, handheld devices or laptop computers.[4,5] Lithium ion batteries are in majority based on non-aqueous liquid organic electrolytes tightly squeezed between two electrodes capable of Li ion intercalation while providing high volumetric and gravimetric energy density as well as low self-discharge rates.[6] The presence of quite distinct electrode–electrolyte interfaces and less defined surfaces of particles in the bulk electrode depending on the electrode porosity and processing facilitates rather complex electrochemical processes inside such batteries, particularly in view of parasitic side reactions, rendering the actually occurring reaction mechanisms poorly understood.[7] Detailed understanding of those phenomena that govern degradation and materials failure upon continued operation, however, is essential in achieving sustainable improvements of efficiency, cycle life and costs, and ideally enables routes to prevent such ageing effects.[8–11]

A proper choice of the electrolyte including a mixture of solvents, necessary additives, and lithium salts positively affects achievable performances of manufactured battery cells and critically determines its (chemical) compatibility with respect to the presence of active or other inactive materials and hence accessible temperature ranges.[12] Moreover, sacrificial decomposition of these non-aqueous electrolytes at low potentials results in passivating surface film formation (the so-called solid electrolyte interphase (SEI)),[13,14] which ideally should avoid electron conduction or tunneling while still permitting Li ion diffusion. Even though this chemical process irreversibly consumes Li ions in the first charging and discharging steps, an effective SEI formation is mandatory for achieving a defined but low cell impedance, long-term cycling stability and reliable electrochemical performance of the cell.[15–17] Since the properties and chemical composition of the SEI depend on the nature of the electrolyte mixture, they may be tailored by applying specific electrolyte components, such as Li salts and electrolyte additives. Commercially available electrolytes typically contain mixtures of cyclic carbonates including diethyl carbonate (DEC), dimethyl carbonate (DMC), ethylene carbonate (EC) or ethyl methyl carbonate (EMC) with suitable Li salts such as lithium hexafluorophosphate ($LiPF_6$).[18] These mixtures operate quite well at room temperature but suffer from degradation at slightly "elevated" temperatures above 35 °C.[19–22] Notably, mere replacement of $LiPF_6$ by lithium difluoro(oxalate)borate (LiDFOB) resulted in increased thermal stabilities.[23–26]

[a] *University of Münster, Institute of Physical Chemistry, 48149 Münster, Germany. E-mail: gbrunklaus@uni-muenster.de*
[b] *University of Münster, MEET Battery Research Center, 48149 Münster, Germany*
[c] *Bruker BioSpin GmbH Silberstreifen, 76827 Rheinstetten, Germany*

† Electronic supplementary information (ESI) available: ^{1}H, ^{7}Li, and ^{19}F diffusion coefficients *via* PFG-NMR. See DOI: 10.1039/c4cp05021e

For several decades, silicon has been considered as promising negative electrode material in lithium ion batteries, mainly because of its high specific capacity of practically *ca.* 3500 mA h g^{-1},[27] thus providing considerably higher energy densities compared to pristine graphite[27–31] and its high abundance in the earth crust. Key problems associated with the use of Si as so called "alloy anode" are the large volume changes of *ca.* 300% and the related poor interfacial stability of Si with the electrolyte thus resulting in poor cycling stability and Coulombic efficiency.[32] Measures to improve the performance include the use of nano-silicon, the mixture of Si with materials that show little volume expansion, for instance carbon and proper choice of electrolyte additives, such as fluoro ethylene carbonate (FEC) which improve the SEI formation and cycling stability.[33–35] In general, further advances in the design of materials for energy storage could be expected from a more thorough understanding of microstructural properties that significantly influence the material function and durability including interfaces, phase boundaries or geometric features (*e.g.*, tortuosity or curvature) – especially when metallic particles or Li "alloys" thereof are involved.[36] In particular, ^{7}Li magnetic resonance imaging (MRI) techniques combined with ^{7}Li *in situ* solid state NMR represent powerful tools to specifically identify localized (electrode surfaces or solid/liquid interphase) or transient (Li ion concentration gradients) material specific processes in batteries under constant current load, thus allowing for evaluation of distinct electrochemical systems and giving insight in actually occurring physical or chemical processes. The great potential of ^{7}Li NMR *in situ* techniques for the investigation of "energy materials" is clearly evidenced by the impressive number of recent reports where changes within electrode materials and electrolyte, ion transport properties, local ion distributions or concentration gradients were identified.[37–44]

Inspired by very recent ^{7}Li 1D NMR imaging measurements of a simplified electrochemical cell (Li//$LiPF_6$(EC/DEC)//Li) at constant current to quantify mass transport in thickened electrolyte mixtures[42] and the observation of gradients of diffusion coefficients,[41] we have examined the applicability of *in situ* ^{7}Li 1D NMR imaging for analysis of electrochemical cells that in view of current progress in battery technology were designed with more realistic components. Therefore, our set-up is based on a nano-silicon–graphite composite electrode *vs.* lithium metal electrode that are separated by glass microfiber filters as host medium for the electrolyte mixture while tuning the contact interfaces by light pressure (Fig. 1).

The resulting cell was then investigated *via* ^{7}Li 1D NMR profiling[45] thereby demonstrating changes of local Li ion concentration upon lithiation of a nano-Si–graphite composite electrode as function of time and surface chemical reaction processes that likely occur in commercially available Li ion batteries. Notably, transient local concentration gradients reflecting SEI formation and different state-of-charge (SOC) conditions could be identified, in addition to improved spatial resolution and signal-to-noise ratio (SNR) due to optimization of the applied pulse program for the ^{7}Li 1D NMR imaging measurements.

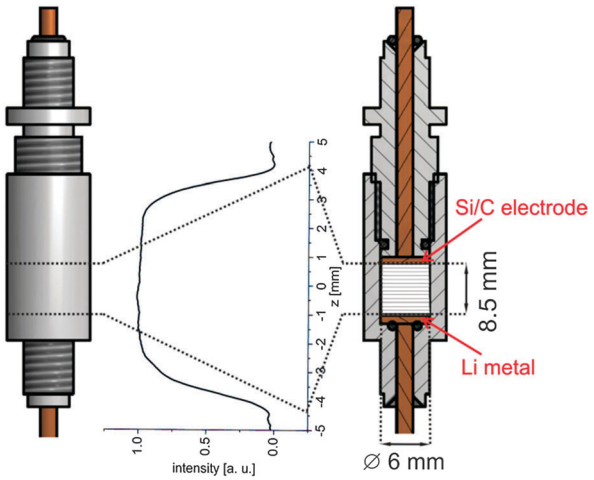

Fig. 1 Design of the cylindrical PTFE cell with a metallic lithium electrode *vs.* nano-Si–graphite composite electrode, including a concentration profile from ^{7}Li 1D NMR Imaging of the as-made cell prior to lithiation.

Experimental

The experimental setup of the electrochemical cell was designed to compromise the conflicting demands concerning chemistry, typical charging procedures and requirements for a ^{7}Li NMR 1D imaging application. Thus, a cylindrical cell with an outer diameter of 10 mm was made from polytetrafluoroethylene (PTFE) taking geometric limitations of the available NMR hardware into account.

Although, PTFE might react with Li in contact with the electrolyte and electrodes to amorphous carbon and lithium fluoride (LiF),[46] no black residues indicating formation of carbon after the application of a constant current load could be detected in the cell so that negligible contribution of this process is assumed under the described electro-chemical measurements conditions and applied time interval. The electrical wiring was achieved *via* copper-based electrodes with two O-rings on each side to ensure sufficient and durable sealing with respect to moisture and ambient atmosphere.

Electrode preparation

The composite electrode (nano-Si–C–CA–binder) was prepared according to a typical recipe: 60 wt% graphite (C) (TIMREX® SFG6, Imerys), 20 wt% nano-silicon powder (nano-Si) (Nano & Amorphous Materials, 50–70 nm), 12 wt% conductive agent (CA) (Super C65, Imerys) and 8 wt% gellan (binder) (Phytagel Sigma Aldrich). Gellan was dissolved in deionized water for 1 h, while the electrode components were dispersed for 20 minutes with 19 000 rpm using a Dispermat® device (VMA). The resulting slurry was then cast on a copper current collector (Carl Schlenk AG®), using a doctor blade with a gap width of 220 μm. Subsequently, the obtained electrodes were dried at 70 °C for 15 min, punched in discs with diameter of 6 mm and finally dried in vacuum at 120 °C for 24 h.

Electrolyte mixture & cell assembly

The electrolyte consists of 1 M lithium difluoro(oxalato)borate (LiDFOB) in a ethylene carbonate (EC) and diethyl carbonate

(DEC) mixture (mass ratio of (3 : 7), and 10 wt% fluoroethylene carbonate (FEC). The electrochemical cell was assembled by at first placing metallic lithium foil (Rockwood Lithium®) on the bottom of the cell, then stacking 13 dried glass microfiber filters (Whatman® GF/D) with a diameter of 6 mm on top. The electrolyte mixture was added so that the separator was fully soaked but avoiding supernatant residues on the topmost separator. Finally, the composite electrode was placed on top and the cell was closed with a defined pressure to ensure an open circuit voltage (OCV) of 2.9 V with 8.5 mm distance between the two electrodes. The cell was assembled in a dry room (residual water content less than 20 ppm), *ca.* 24 h prior to insertion into the NMR Imaging probe.

Electrochemical measurements & SEM

After successful wiring and insertion to the NMR probe, the cell was treated under a constant current (CC) load of 20 μA, corresponding to a charging rate of $\approx C/13$ based on the electrode mass loading taking graphite and silicon as active material into account. The CC experiment was performed over a time of 18 h to allow for a lithiation of the composite electrode and subsequent Li plating. The electrochemical treatment was performed applying a Solartron SI 1287 potentiostat/galvanostat. The discharged cell was disassembled in a glove box (MBraun) under argon atmosphere; the lithiated electrode was carefully washed with dimethyl carbonate (DMC) and transported to the SEM without contact to ambient atmosphere. A ZEISS Auriga scanning electron microscope was used to investigate the particle morphology and the surface of the electrode materials. In order to prevent the electrodes from damage or changes of the original structure, the investigations were carried out at low accelerating voltages and without sputtering.

NMR & ^{7}Li imaging experiments

^{7}Li 1D NMR imaging measurements were performed on a Bruker Avance III HD 500 MHz spectrometer equipped with Bruker micro-imaging accessory including a GREAT-60 amplifier and a Bruker DIFF50 probe with a *z*-gradient of max. 28.5 T m^{-1} (at Bruker, Rhein-stetten/Germany). The ^{7}Li 1D NMR images were recorded with a 10 mm coil operating at a constant temperature of 23 °C. In addition, PFG NMR diffusion data was obtained at the MEET battery research center with a Bruker Avance III 200 MHz spectrometer operating a Bruker GREAT-60 unit and Bruker DIFF30 probe with a *z*-gradient of max. 17.1 T m^{-1}. Diffusion measurements to determine the free diffusion constants of ^{1}H, ^{7}Li, and ^{19}F, respectively, of the electrolyte mixture (both pristine liquid and soaked in Whatman® GF/D separators) were carried out at a constant temperature of 23 °C. All one-dimensional profiles were acquired by a 1D ^{7}Li spin-echo imaging sequence that is comprised of a classic Hahn echo[47] (pi/2–tau–pi–tau) and two magnetic field gradient pulses (with amplitude g, duration δ, separated by Δ).[48] Ideally, the excitation and refocussing pulses generate a rectangular profile, that is, with defined starting and ending point in space,[49] provided that local spin density fluctuations due to concentration gradients or otherwise produced heterogeneity can be ruled out. Though shaped pulses are often applied in imaging applications (*e.g.*, to boost the signal intensity), rectangular pulses in principle allow for shorter pulse lengths and thus improved pulse excitation profiles.[50] In such cases, the robustness of the refocussing π-pulse with respect to any radio-frequency offsets may be improved by the use of composite π-pulses such as $(\pi/2)_\varphi(3\pi/2)_{\varphi+\pi}$ that are rather simple but essential components of so-called symmetry based NMR sequences (Fig. 2).[51]

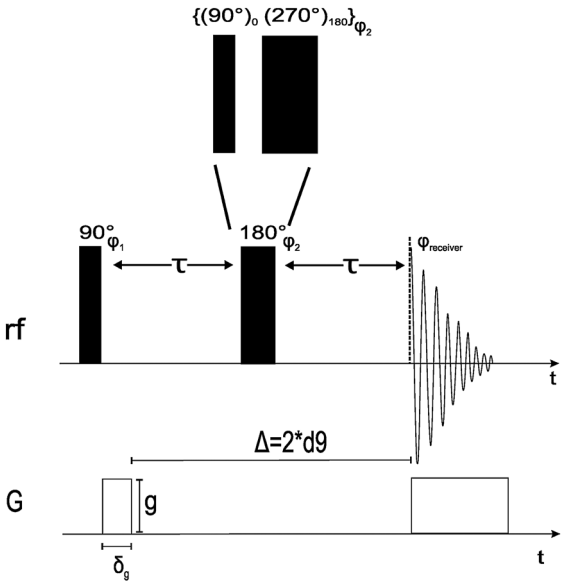

Fig. 2 Schematic description of a spin echo pulse sequence with a pulsed gradient. The time between the 90° and 180° pulses is denoted as τ; gradient strength and gradient duration are described by g and δ while the time scale between both gradient pulses is given by Δ. For improved results, the single rectangular 180° pulse is replaced by a composite pulse {(90°) (270°)}; note that a phase presetting delay of 0.3 μs is required to avoid receiver problems. In contrast to the initially applied phase cycling, the modified phase cycling selects detectable single-quantum coherences ($\Delta p = \pm 1$) based on the 90° pulse, taking merely the sign reversal effect of the 180° pulse into account for the setting of the receiver phase. Note that any further coherence selection ($\Delta p = \pm 2$) with the 180° pulse did not improve the quality of the 1D profile. The data was recorded with the phases $\varphi_1 = (x,-x,y,-y,-x,x,-y,y)$, $\varphi_2 = (x)$ and $\varphi_{receiver} = (x,-x,-y,y,-x,x,y,-y)$. The gradient stabilization time (d2) was 100 μs, the dephasing time (d18) was set to 1.28 ms (*cf.* ESI†).

The 90° pulse length was set to 12 μs (corresponding to an rf-field of 20.8 kHz), 128 transients were recorded at a repetition time of 3 s and a gradient strength of 0.75 T m^{-1}. The distance between the 90° and composite 180° pulse was about 1.5 ms yielding an echo time of 3 ms. Since metallic lithium and lithium ions "immobilized" within the electrode or SEI have significantly shorter transverse relaxation times ($T_2 \leq 1$ ms) than rather "freely" diffusing lithium ions in the electrolyte ($T_2 \gg 1$ ms), the concentration profile will be dominated by more mobile lithium species.[42] In principle, likely monitoring of lithium ions that enter the electrolyte/electrode interface could be feasible provided that sufficiently large gradient strengths (more than 3 T m^{-1}) are tolerated by the probe and cell setup so that reduced echo times were available. The pulse phase cycling that allows for single-quantum coherence selection (representing the detectable

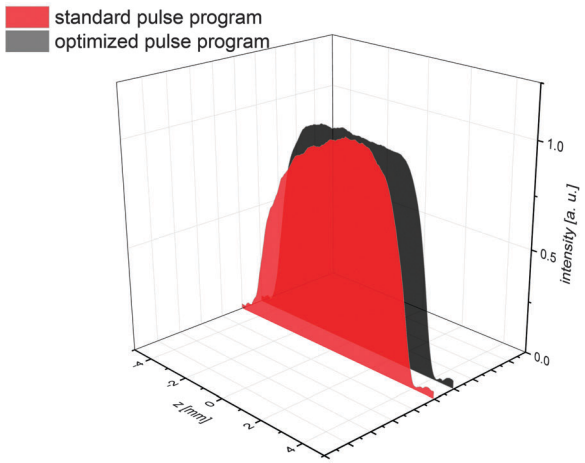

Fig. 3 ^{7}Li 1D NMR imaging measurements before and after pulse program optimization, resulting in a more rectangular profile in agreement with the anticipated flat Li^{+} distribution in the *in situ* cell in the absence of applied current or convection.

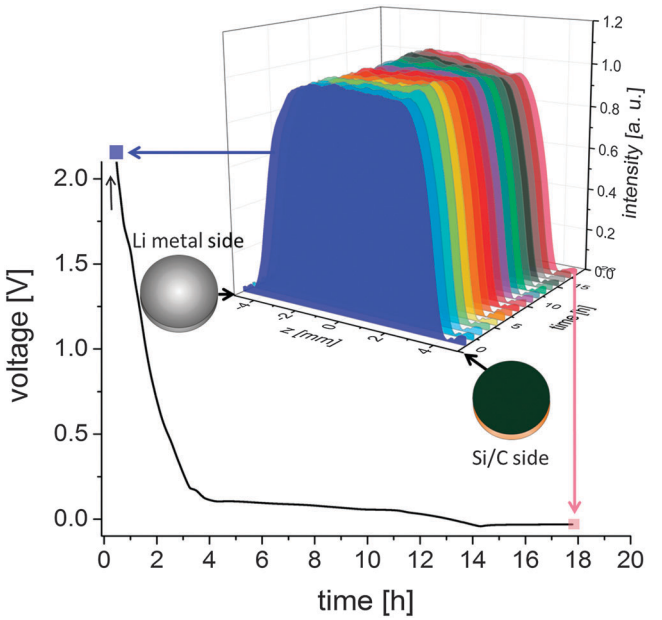

Fig. 4 Voltage *vs.* time plot of the Li/Si–C electrochemical cell during the *in situ* ^{7}Li NMR imaging measurements under discharge at a constant current of 20 μA. After 13 hours of lithium uptake into the nano-Si–graphite composite Li plating could be monitored. Selected 1D NMR profiles during the course of the measurement are shown in the insert indicating the concentration of Li ion (intensity [a.u.]), spatial position (*z* [mm]), and time or SOC (time [h]).

NMR signal) was reduced and solely done with the 90° pulse since the 180° pulse of the echo simply inverts the sign of the coherence and thus does not require further selection. In fact, consideration of artefact correction based on the well-known four-step CYCLOPS phase cycling of the 180° pulse did not improve the quality of the ^{7}Li NMR profile. The benefit of the applied NMR pulse program compared to a previously used version without further optimization is documented in Fig. 3.

Clearly, a more rectangular profile anticipated for the utilized battery cell design could be achieved except for the often observed curvature of the concentration profile at or near interfaces (*e.g.* among liquid electrolyte and a solid electrode surface) that reflect variations of the radiofrequency field strength and sensitivity along the *z*-direction.[52] Each single concentration profile comprises 128 scans with a recycle delay of 3 s (384 s per profile). In view of the total duration of the experiment of about 18 h and the rather low current of 20 μA applied during discharge, the recorded concentration profiles approximately represent steady states of the cell. Note that a spatial resolution of 35.2 μm per pt was achieved.

Data processing

The NMR data was acquired and processed with Bruker Topspin 3.0 software while additional data processing was performed with Origin Pro 9.1 (Origin Lab). The obtained ^{7}Li concentration profiles were smoothed using Savitzky–Golay filter (with 25 points), a permissible and appropriate mathematical method to improve the signal to noise ratio without distorting the original signal.[53] For the sake of clarity particular steps of the acquired concentration profiles are omitted considering only spectra recorded after every 30 minutes in the Results and discussion section.

Results and discussion

The voltage of the cell designed for the *in situ* ^{7}Li NMR imaging experiment during discharge under a constant current of 20 μA is shown in Fig. 4. Several plateaus between 2 and 0 V could be observed that indicate electrochemical processes occurring inside the cell including partial decomposition of the electrolyte due to SEI formation and structural changes of the electrode during lithium intercalation into graphite and lithium alloying with Si (which is known to be particularly complex in the presence of nano-structured electrode components).[54] Note that the experimentally achieved capacity of the considered cell corresponds well to the theoretical capacity of 263 ± 6 μA h calculated from the mass loading of 0.22 ± 0.01 mg determined for the electrode thus indicating a sufficient functionality of the electrochemical setup.

The first plateau around 1.6–1.5 V (Fig. 4 and 5) is attributed to partial decomposition of the liquid electrolyte, mainly LiDFOB forming a decomposition surface layer on the anode, which is in agreement with previous results.[55–57] Further plateaus around 1.2 and 0.5 V indicate (continued) consumption of the carbonate solvents due to SEI formation (see dQ/dV plot in Fig. 5).[35,58–63] The dominating reaction represented by the following plateaus below 0.25 V are the intercalation of lithium ions into graphite at different stages (Li_xC_6), resulting into LiC_6 in case of full lithiation.[15,64,65] Upon cycling, the at first rather crystalline nano-structured silicon embedded in the composite electrode typically cracks due to volume expansion.[31] It is known, that crystalline Si converts into an amorphous state during lithiation.[66,67] The change to an amorphous state, however, proceeds without any visible plateaus in the voltage curve. During constant current discharge silicon is expected to form the

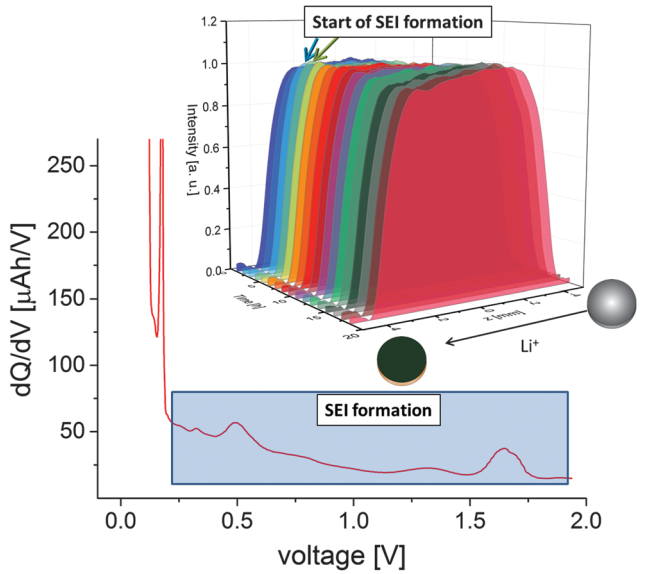

Fig. 5 Overview of the Li concentration profiles acquired during lithiation of the nano-Si–graphite composite electrode under constant current discharge with 20 µA, reflecting localized changes of the Li ion distribution. Note the initial increase in Li concentration during SEI formation, most likely due to partially impaired ion flux into the composite electrode. The corresponding section (cut-out) of the dQ/dV plot indicating the partial decomposition of electrolyte components resulting in SEI formation is shown on the bottom (the other dQ/dV part is omitted for clarity).

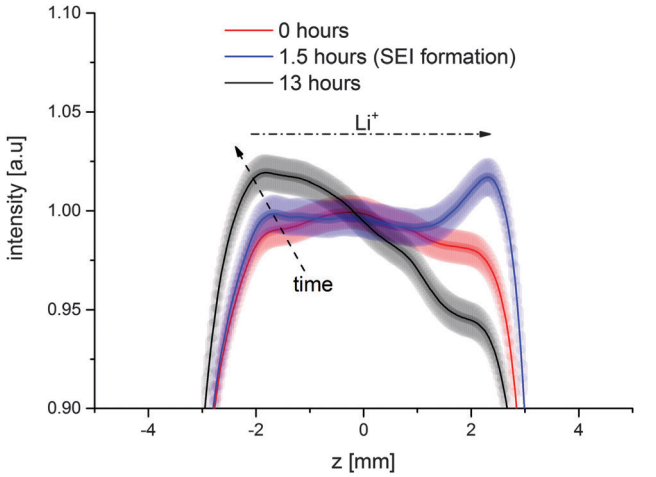

Fig. 6 Overview of 3 Li concentration profiles acquired during lithiation of the nano-Si–graphite composite electrode at the pristine condition (t = 0 h), under constant current discharge with 20 µA (t = 1.5 h) and at the fully lithiated state of the composite anode (t = 13 h), reflecting localized changes of the Li ion distribution taking uncertainties into account (shown as shadow to the corresponding Li ion profiles). The SNR ratio was calculated based on the mean value of 15 points of the noise and determined for every data point of every Li concentration profile. Note that uncertainties for the 2D figure due to the application of an additional smoothing with 25 point were also considered for the shown error bars.

$Li_{15}Si_4$ phase below *ca.* 40 mV,[37,66,68,69] which in principle is also monitored by characteristic ^{7}Li (or ^{29}Si) solid state NMR chemical shifts.[70,71]

The electrochemical processes occurring during the constant current discharge such as electrolyte decomposition and SEI formation can be independently monitored by the 1D ^{7}Li NMR imaging profiles that reflect the local lithium ion distribution and thus the course of the lithium concentration. The first 1D profile of the cell prior to discharge (blue profile in Fig. 4) resembles a flat Li concentration distribution anticipated for a homogeneous spread of the electrolyte mixture within the separator stack, except for the typically observed slight curvature towards the edges of the profile due to susceptibility effects at the Li metal–electrolyte and Si–C electrode–electrolyte interfaces (Fig. 5).

Since the ^{7}Li self-diffusion coefficients (independently obtained from PFG NMR measurements) of both pristine liquid electrolyte mixture [D = 1.53 × 10^{-10} m^2 s^{-1}] and the one soaked within the separator stack [D = 1.33 × 10^{-10} m^2 s^{-1}] differ about 15%, possible contributions from convection cannot be excluded, though in practice disturbing effects were not identified. When switching on a constant current of 20 µA, the ^{7}Li NMR Imaging profiles start to change along the electric field (in z-direction) and the occurrence of concentration gradients could be monitored. Notably, at early stages of the experiment, an increase of the local Li ion concentration at the nano-Si/graphite electrode surface of (2 ± 0.5%) indicates the accumulation of charge carriers during and shortly after the formation of a decomposition layer (SEI), most likely due to a temporarily impaired flux of Li ions into the anode. This observation suggests that during partial decomposition of electrolyte components Li ions in a diamagnetic environment accumulate at the interphase between electrolyte and electrode forming a temporary bottleneck. After completion of the protective layer at the anode (resulting from partial decomposition of electrolyte components) and onset of Li intercalation into graphite at a cell voltage of 250 mV,[72] the Li concentration profile at the anode site flattens again hinting at the recovery of rather unperturbed Li ion flux into the anode.

Fig. 6 illustrates significant differences in local Li concentration during SEI formation compared to the Li ion distribution of both the pristine cell and after 13 hours (completely lithiated anode) taking uncertainties due to the signal to noise ratio (SNR) and smoothing function into account. Indeed, local changes reflecting the partial decomposition of the electrolyte are clearly visible while the impact of rf-inhomogeneity on the signal intensities on the anode side can be excluded since otherwise the increase would also be present in the other profiles at different SOCs (Fig. 6).

A schematic model of the electrochemical processes resulting in local changes of Li ion concentration due to SEI formation is shown in Fig. 7 indicating a local agglomeration of Li species at the composite electrode–electrolyte interphase. After that, the Li concentration profiles revealed a decrease of mass density at the nano-Si–graphite composite electrode accompanied by an increased mass density at the Li metal electrode. When the electrode was lithiated and in the presence of plated Li, a clear increase in Li ion concentration and therefore a higher mass density at the Li metal electrode at the expense of a lower mass density at Si/graphite electrode was found (Fig. 5).

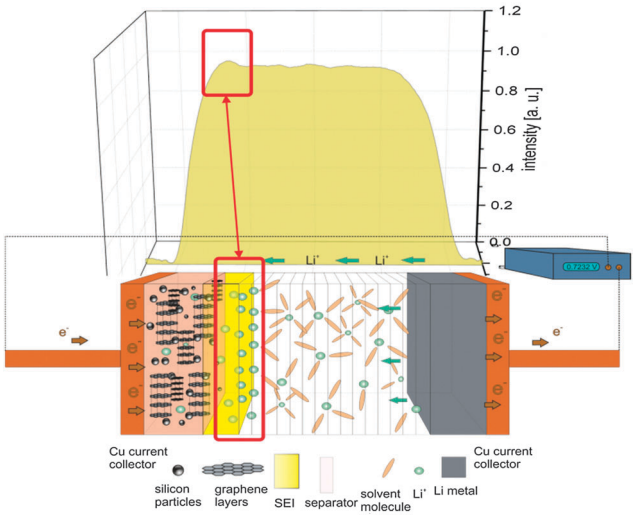

Fig. 7 Schematic model explaining the Li^+ agglomeration during the SEI formation at the Si/graphite electrode observed in ^7Li NMR imaging profiles at a voltage of around 0.7 V *vs.* Li/Li^+.

Notably, at the end of the discharge step after 18 h, the corresponding Li ion concentrations at the Li metal and the composite Si/graphite electrode differ by (15 ± 0.6)% thereby documenting that significant changes of the local ion concentration predominantly occur in the proximity of electrode surfaces while the middle part of the cell (where the electrolyte reservoir is) remains rather unchanged, in good agreement with the boundary conditions of the Maxwell–Stefan equation.[43,73]

A SEM image of the composite electrode after full lithiation clearly confirms the presence of a decomposition layer on the surface of the electrode (Fig. 8), thus corroborating partial decomposition of the electrolyte during the discharge process (commonly denoted as SEI formation[74]).

For further refinement of molecular models describing ion transport in multicomponent systems, the quantitative knowledge of diffusion coefficients and other transport properties is required. However, the extraction of *e.g.* transport numbers from Li concentration profiles is fairly difficult to achieve and with reasonable effort rather limited to simpler cases.[75] In case of a concentrated electrolyte comprised of a binary salt and a mixture of two solvents a simplified approximation of 1 M $LiPF_6$ in a 1 : 1 mixture of EC/DEC, thickened with 15 wt% PMMA) transport parameters could be successfully estimated from ^7Li 1D NMR Imaging profiles of a electrochemical model cell.[42] Though in principle, concentration profiles may be derived from the Maxwell–Stefan and mass balance equations, taking only the *z*-direction into account,[73,76,77] the theory is strictly valid for fluids only and may not represent a good approximation for rather viscous electrolytes that are preferred to avoid leakage of batteries. In addition, the Maxwell–Stefan diffusivities do not correspond to Fick's diffusion coefficients and thus are not straightforward accessible. Nevertheless, adopting the reported model,[42] describing the time-dependent Li concentration profile by a partial differential equation and taking components of the electrolyte mixture (carbonates and Li salt) and the presence of the separator stack into account, we obtain eqn (1):[77,78]

$$\varepsilon\frac{\partial c_{\mathrm{LiDFOB}}}{\partial t} = \frac{\partial}{\partial z}\left[\left(1 - c_{\mathrm{LiDFOB}} V_{\mathrm{m}}^{\mathrm{LiDFOB}}\right)\cdot\left(\left(1 + \frac{\partial \ln \alpha_{\pm}}{\partial \ln c_{\mathrm{LiDFOB}}}\right) \times \frac{c_{\mathrm{tot}}}{c_{\mathrm{EC-DEC-FEC}}}\varepsilon^{\beta} D_{\mathrm{LiDFOB}}\frac{\partial c_{\mathrm{LiDFOB}}}{\partial z} + \frac{\left(1 - t_{+}^{\mathrm{EC-DEC-FEC}}\right)}{F} i\right)\right] \quad (1)$$

where $\alpha_{\pm}$ is the salt activity coefficient, ε and β are the Bruggeman coefficient and the porosity of the glass microfiber separator, while the transport number of Li ions that are coordinated to cyclic carbonates is $t_{+}^{(\mathrm{EC-DEC-FEC})}$. To solve this equation numerically, quite reasonable starting values of the parameters are required. Due to the complexity of the electrochemical cell based on technically relevant components in view of real lithium ion battery application including three carbonate moieties (solvents), less-defined surface and inter-phases at the nano-Si–graphite composite electrode compared to Li metal and hence complex pathways of Li ion flux into the electrode (particularly in view of the presence of binder),[79] local changes of the charge carrier concentration or even partial molar volumes, the required parameters are not always accessible and up to now could not unambiguously be extracted with numerical methods.[80–82] Also, excess-electron induced reactions and resulting intermediate species from electrolyte decomposition and its role for the formation of passivating layers during battery operation were considered in the framework of density functional theory (DFT) computations, but the approach is limited to idealized systems.[61] Since appropriate models with respect to the complexity of both the applied electrolyte mixture and composite electrode and the electrochemical conditions are not yet available, we refrain from a fully quantitative analysis of the recorded ^7Li 1D NMR profiles containing the spatial distribution of Li ions as a function of time and the state of charge. Finally, ^1H, ^{19}F and ^7Li self-diffusion coefficients of the pristine and the electrolyte mixture soaked in the separator stack were derived from PFG NMR (ESI†). Compared to the reported changes in the Li concentration profile with similar setup and current densities[42]

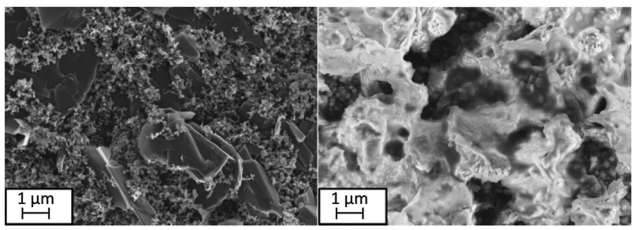

Fig. 8 SEM image of a pristine nano-Si–graphite composite electrode (left). Particles with a size of 3 µm represent graphite, while the smaller spherically shaped particles can be attributed to nano-Si (50–70 nm). The smallest particles are the conductive carbon black additive. The composite electrode after SEI formation and the first discharge (harvested from the used electro-chemical cell) is shown at the right.

the relative concentration changes in our case are less pronounced, which may be due to the application of glass fiber separator material where essentially the amount of electrolyte per volume soaked in the separator is lower than the volume unit filled with pure electrolyte. In addition, it appears reasonable that a different relative permittivity based on the chosen electrolyte composition also affects observable signal intensities in the measured Li concentration profiles.

Summary and conclusion

In this work we have demonstrated the potential of ^{7}Li 1D NMR imaging towards real battery application to identify lithium ion concentration gradients under constant current conditions. A home-made PTFE cell based on a stack of glass microfiber separators soaked with an electrolyte mixture that is relatively stable at elevated temperatures squeezed between a Li metal electrode and a nano-Si–graphite composite electrode was constructed and showed sufficient electrochemical performance. ^{7}Li 1D *in situ* NMR profiles could be obtained with an improved NMR pulse sequence as function of time and state of charge, thereby, visualizing the course of lithium ion concentration during discharge. Surface localized changes of Li concentration were attributed to processes such as SEI formation or full lithiation of the composite electrode, in principle allowing extraction of transport properties depending on the applied currents. Molecular understanding of transient surface processes is of significance for further improvement of performance and cycling stability of future Li ion batteries, particularly to unravel the impact of electrolyte additives on the electrolyte decomposition, the SEI, as well as the interface and surface behaviour and of course in the lithium ion mobility. This study strongly focussed on ''real'' battery components with respect to current industrial lithium ion battery applications. Simpler electrolyte mixtures or electrode compositions that would facilitate access to more quantitative analysis or detailed separation of lithium incorporation or release processes are planned for the future.

Acknowledgements

Funding from the Deutsche Forschungsgemeinschaft (DFG) within the project ''WeNDeLIB (SSP 1473)'' is gratefully acknowledged. We appreciate valuable discussions with the members of this project. Also, the authors are indebted to Bruker (Rheinstetten, Germany) for providing access to NMR equipment, their time, and interest in the project, including illuminative discussions with D. Gross. We thank M. Amereller (MEET, Uni Münster) for donating the LiDFOB salt used in this study.

References

1 F. T. Wagner, B. Lakshmanan and M. F. Mathias, *J. Phys. Chem. Lett.*, 2010, **1**, 2204–2219.
2 J. B. Goodenough, *Acc. Chem. Res.*, 2013, **46**, 1053–1061.
3 R. Wagner, N. Preschitschek, S. Passerini, J. Leker and M. Winter, *J. Appl. Electrochem.*, 2013, **43**, 481–496.
4 M. Winter and R. J. Brodd, *Chem. Rev.*, 2004, **104**, 4245–4270.
5 J. B. Goodenough and K.-S. Park, *J. Am. Chem. Soc.*, 2013, **135**, 1167–1176.
6 J. Chun, M. Chung, J. Lee and Y. Kim, *Phys. Chem. Chem. Phys.*, 2013, **15**, 7036–7040.
7 K. Xu and A. von Cresce, *J. Mater. Chem.*, 2011, **21**, 9849–9864.
8 J. Vetter, P. Novák, M. R. Wagner, C. Veit, K. C. Möller, J. O. Besenhard, M. Winter, M. Wohlfahrt-Mehrens, C. Vogler and A. Hammouche, *J. Power Sources*, 2005, **147**, 269–281.
9 M. Broussely, S. Herreyre, P. Biensan, P. Kasztejna, K. Nechev and R. J. Staniewicz, *J. Power Sources*, 2001, **97–98**, 13–21.
10 V. Agubra and J. Fergus, *Materials*, 2013, **6**, 1310–1325.
11 S. C. Nagpure, B. Bhushan and S. S. Babu, *J. Electrochem. Soc.*, 2013, **160**, A2111–A2154.
12 V. Etacheri, R. Marom, R. Elazari, G. Salitra and D. Aurbach, *Energy Environ. Sci.*, 2011, **4**, 3243–3262.
13 P. Verma, P. Maire and P. Novák, *Electrochim. Acta*, 2010, **55**, 6332–6341.
14 M. R. Wagner, P. R. Raimann, A. Trifonova, K. C. Moeller, J. O. Besenhard and M. Winter, *Electrochem. Solid-State Lett.*, 2004, **7**, A201–A205.
15 M. Winter, J. O. Besenhard, M. E. Spahr and P. Novák, *Adv. Mater.*, 1998, **10**, 725–763.
16 M. Winter and J. O. Besenhard, *Chem. Unserer Zeit*, 1999, 252–266.
17 M. Winter and J. O. Besenhard, *Chem. Unserer Zeit*, 1999, 320–332.
18 K. Xu, *Chem. Rev.*, 2004, **104**, 4303–4418.
19 C. L. Campion, W. Li and B. L. Lucht, *J. Electrochem. Soc.*, 2005, **152**, A2327–A2334.
20 L. Terborg, S. Weber, F. Blaske, S. Passerini, M. Winter, U. Karst and S. Nowak, *J. Power Sources*, 2013, **242**, 832–837.
21 B. Ravdel, K. M. Abraham, R. Gitzendanner, J. DiCarlo, B. Lucht and C. Campion, *J. Power Sources*, 2003, **119–121**, 805–810.
22 T. Kawamura, S. Okada and J.-I. Yamaki, *J. Power Sources*, 2006, **156**, 547–554.
23 L. Zhou, W. Li, M. Xu and B. Lucht, *Electrochem. Solid-State Lett.*, 2011, **14**, A161–A164.
24 M. Xu, L. Zhou, L. Hao, L. Xing, W. Li and B. L. Lucht, *J. Power Sources*, 2011, **196**, 6794–6801.
25 J. L. Allen, S.-D. Han, P. D. Boyle and W. A. Henderson, *J. Power Sources*, 2011, **196**, 9737–9742.
26 S. Zugmann, D. Moosbauer, M. Amereller, C. Schreiner, F. Wudy, R. Schmitz, R. Schmitz, P. Isken, C. Dippel, R. Müller, M. Kunze, A. Lex-Balducci, M. Winter and H. J. Gores, *J. Power Sources*, 2011, **196**, 1417–1424.
27 M. N. Obrovac and L. J. Krause, *J. Electrochem. Soc.*, 2007, **154**, A103–A108.
28 C.-M. Park, J.-H. Kim, H. Kim and H.-J. Sohn, *Chem. Soc. Rev.*, 2010, **39**, 3115–3141.
29 G. X. Wang, J. H. Ahn, J. Yao, S. Bewlay and H. K. Liu, *Electrochem. Commun.*, 2004, **6**, 689–692.

30 U. Kasavajjula, C. Wang and A. J. Appleby, *J. Power Sources*, 2007, **163**, 1003–1039.
31 J.-I. Lee, J.-H. Park, S.-Y. Lee and S. Park, *Phys. Chem. Chem. Phys.*, 2013, **15**, 7045–7049.
32 W.-R. Liu, N.-L. Wu, D.-T. Shieh, H.-C. Wu, M.-H. Yang, C. Korepp, J. O. Besenhard and M. Winter, *J. Electrochem. Soc.*, 2007, **154**, A97–A102.
33 N.-S. Choi, K. H. Yew, K. Y. Lee, M. Sung, H. Kim and S.-S. Kim, *J. Power Sources*, 2006, **161**, 1254–1259.
34 I. A. Profatilova, C. Stock, A. Schmitz, S. Passerini and M. Winter, *J. Power Sources*, 2013, **222**, 140–149.
35 D. Mazouzi, N. Delpuech, Y. Oumellal, M. Gauthier, M. Cerbelaud, J. Gaubicher, N. Dupré, P. Moreau, D. Guyomard, L. Roué and B. Lestriez, *J. Power Sources*, 2012, **220**, 180–184.
36 A. P. Cocco, G. J. Nelson, W. M. Harris, A. Nakajo, T. D. Myles, A. M. Kiss, J. J. Lombardo and W. K. S. Chiu, *Phys. Chem. Chem. Phys.*, 2013, **15**, 16377–16407.
37 B. Key, R. Bhattacharyya, M. Morcrette, V. Seznéc, J.-M. Tarascon and C. P. Grey, *J. Am. Chem. Soc.*, 2012, **131**, 9239–9249.
38 S. Chandrashekar, N. M. Trease, H. J. Chang, L.-S. Du, C. P. Grey and A. Jerschow, *Nat. Mater.*, 2012, **11**, 1–5.
39 R. Bhattacharyya, B. Key, H. Chen, A. S. Best, A. F. Hollenkamp and C. P. Grey, *Nat. Mater.*, 2010, **9**, 504–510.
40 R. Chandrasekaran, A. Magasinski, G. Yushin and T. F. Fuller, *J. Electrochem. Soc.*, 2010, **157**, A1139–A1151.
41 S. A. Krachkovskiy, A. D. Pauric, I. C. Halalay and G. R. Goward, *J. Phys. Chem. Lett.*, 2013, **4**, 3940–3944.
42 M. Klett, M. Giesecke, A. Nyman, F. Hallberg, R. W. Lindström, G. Lindbergh and I. Furó, *J. Am. Chem. Soc.*, 2012, **134**, 14654–14657.
43 M. Giesecke, S. V. Dvinskikh and I. Furó, *J. Magn. Reson.*, 2013, **226**, 19–21.
44 K. Ogata, E. Salager, C. J. Kerr, A. E. Fraser, C. Ducati, A. J. Morris, S. Hofmann and C. P. Grey, *Nat. Commun.*, 2014, **5**, 1–11.
45 J. Leisen, I. J. Gomez, J. A. Roper III, J. C. Meredith and H. W. Beckham, *ACS Comb. Sci.*, 2012, **14**, 415–424.
46 W. Liu, X. Huang, L. Guobao, Z. Wang, H. Huang, L. Zhonghua, R. Xue and L. Chen, *J. Power Sources*, 1997, **68**, 344–347.
47 E. Hahn, *Phys. Rev.*, 1950, **80**, 580–594.
48 P. T. Callaghan, A. Coy, D. MacGowan, K. J. Packer and F. O. Zelaya, *Nature*, 1991, **351**, 467–469.
49 B. A. Jung and M. Weigel, *J. Magn. Reson. Imaging*, 2013, **37**, 805–817.
50 J. A. Tang, G. Zhong, S. Dugar, J. A. Kitchen, Y. Yang and R. Fu, *J. Magn. Reson.*, 2012, **225**, 93–101.
51 M. Carravetta, M. Edén, X. Zhao, A. Brinkmann and M. H. Levitt, *Chem. Phys. Lett.*, 2000, **321**, 205–215.
52 D. I. Hoult, *Prog. Nucl. Magn. Reson. Spectrosc.*, 1978, **12**, 41–77.
53 A. Savitzky and M. J. E. Golay, *Anal. Chem.*, 1964, **36**, 1627–1639.
54 J. Jamnik and J. Maier, *Phys. Chem. Chem. Phys.*, 2003, **5**, 5215–5220.
55 J. Liu, Z. Chen, S. Busking and K. Amine, *Electrochem. Commun.*, 2007, **9**, 475–479.
56 Z. Chen, Y. Qin, J. Liu and K. Amine, *Electrochem. Solid-State Lett.*, 2009, **12**, A69–A72.
57 Z. Chen, J. Liu and K. Amine, *Electrochem. Solid-State Lett.*, 2007, **10**, A45–A47.
58 R. Imhof and P. Novák, *J. Electrochem. Soc.*, 1998, **145**, 1081–1087.
59 S.-K. Jeong, M. Inaba, R. Mogi, Y. Iriyama, T. Abe and Z. Ogumi, *Langmuir*, 2001, **17**, 8281–8286.
60 J. S. Kim, D. Byun and J. K. Lee, *Curr. Appl. Phys.*, 2014, **14**, 596–602.
61 K. Leung, S. B. Rempe, M. E. Foster, Y. Ma, J. M. Martinez del la Hoz, N. Sai and P. B. Balbuena, *J. Electrochem. Soc.*, 2014, **161**, A213–A221.
62 K. Leung, *Chem. Phys. Lett.*, 2013, **568–569**, 1–8.
63 I. A. Profatilova, T. Langer, J. P. Badillo, A. Schmitz, H. Orthner, H. Wiggers, S. Passerini and M. Winter, *J. Electrochem. Soc.*, 2012, **159**, A657–A663.
64 M. Letellier, F. Chevallier, F. Béguin, E. Frackowiak and J.-N. Rouzaud, *J. Phys. Chem. Solids*, 2004, **65**, 245–251.
65 R. Fong, U. von Sacken and J. R. Dahn, *J. Electrochem. Soc.*, 1990, **137**, 2009–2013.
66 M. N. Obrovac and L. Christensen, *Electrochem. Solid-State Lett.*, 2004, **7**, A93–A96.
67 J. Li and J. R. Dahn, *J. Electrochem. Soc.*, 2007, **154**, A156.
68 M. Holzapfel, H. Buqa, L. J. Hardwick, M. Hahn, A. Würsig, W. Scheifele, P. Novák, R. Kotz, C. Veit and F. Petrat, *Electrochim. Acta*, 2006, **52**, 973–978.
69 N. S. Hochgatterer, M. R. Schweiger, S. Koller, P. R. Raimann, T. Wöhrle, C. Wurm and M. Winter, *Electrochem. Solid-State Lett.*, 2008, **11**, A76–A80.
70 J.-H. Trill, C. Tao, M. Winter, S. Passerini and H. Eckert, *J. Solid State Electrochem.*, 2011, **15**, 349–356.
71 A. S. Cattaneo, S. Dupke, A. Schmitz, J. P. Badillo, M. Winter, H. Wiggers and H. Eckert, *Solid State Ionics*, 2013, **249–250**, 41–48.
72 D. Billaud, F. Henry and P. Wellmann, *Mol. Cryst. Liq. Cryst. Sci. Technol., Sect. A*, 1994, **245**, 159–164.
73 C. F. Curtiss and R. B. Bird, *Ind. Eng. Chem. Res.*, 1999, **38**, 2515–2522.
74 M. Winter, *Z. Phys. Chem.*, 2009, **223**, 1395–1406.
75 A. Nyman, M. Behm and G. Lindbergh, *Electrochim. Acta*, 2008, **53**, 6356–6365.
76 R. Taylor and R. Krishna, *Multicomponent mass transfer*, Wiley, New York, 1993, vol. 597.
77 A. Nyman, M. Behm and G. Lindbergh, *J. Electrochem. Soc.*, 2011, **158**, A628–A635.
78 A. Nyman, M. Behm and G. Lindbergh, *J. Electrochem. Soc.*, 2011, **158**, A636–A643.
79 S.-L. Chou, Y. Pan, J.-Z. Wang, H.-K. Liu and S.-X. Dou, *Phys. Chem. Chem. Phys.*, 2014, **16**, 20347–20359.
80 M. W. Verbrugge and B. J. Koch, *J. Electrochem. Soc.*, 1996, **143**, 600–608.
81 G. G. Botte, V. R. Subramanian and R. E. White, *Electrochim. Acta*, 2000, **45**, 2595–2609.
82 J. Bisquert, *Phys. Chem. Chem. Phys.*, 2008, **10**, 49–72.